

**SWISS PLASMA  
CENTER**

## Master thesis

---

PIC Electrostatic Simulations of Electron  
Trapping near the Cathode of Gyrotron  
Electron Guns.

---

Patryk Kamiński

*Supervisors :*

Dr. Stefano Alberti

Dr. Trach-Minh Tran

Jérémy Genoud

*External expert :*

Dr. Ioannis Gr. Pagonakis

June 22, 2017

## Contents

<b>1</b>	<b>Introduction</b>	<b>3</b>
1.1	Motivation . . . . .	3
1.2	Electrostatic PIC model . . . . .	4
1.3	Normalization . . . . .	6
<b>2</b>	<b>Numerical technique</b>	<b>9</b>
2.1	Poisson equation . . . . .	9
2.2	Momentum equation . . . . .	12
2.2.1	Borris method . . . . .	12
2.2.2	Details of calculations . . . . .	14
<b>3</b>	<b>Implementation</b>	<b>18</b>
3.1	Initialization . . . . .	18
3.2	Poisson equation solver . . . . .	20
3.2.1	Case of empty space between metallic walls . . . . .	22
3.2.2	Thin layer of electron plasma . . . . .	26
<b>4</b>	<b>Particles mover</b>	<b>30</b>
4.1	Magnetic field topology . . . . .	30
4.2	Mirror effect . . . . .	31
4.3	Penning mechanism . . . . .	34
<b>5</b>	<b>Electron plasma simulation</b>	<b>37</b>
5.1	Electron plasma with $\frac{\omega_{ce}}{\omega_{pe}} = 8.81$ . . . . .	37
5.2	Electron plasma with $\frac{\omega_{ce}}{\omega_{pe}} = 3.11$ . . . . .	41
<b>6</b>	<b>Conclusions</b>	<b>45</b>

# 1 Introduction

## 1.1 Motivation

The gyrotron is a wave source device widely used in plasma heating systems. Its operation is based on the electron cyclotron resonance maser (CRM) instability. The kinetic energy of electron beam is converted into an electromagnetic wave in a cylindrical cavity. Beam electrons are produced by thermal emission of heated ring placed on the magnetron injection gun (MIG). After emission, electrons are accelerated by externally applied voltage and guided by magnetic field to form required gyro-motion.

In practice, the operation of the electron gun is influenced by many factors that are not always taken into account in design phase. Some effects can significantly reduce the efficiency of the gyrotron [3]. Experimental evidences [3], have shown that electrons can be trapped in the magnetic potential well near the cathode of electron gun.

So called, Penning mechanism takes place wherever magnetic field lines intersect equipotential lines like it is shown on the figure (1). The electrons are guided by magnetic field lines and experience force due to parallel component of electric field  $\vec{F} = -e\vec{E}_{\parallel}$  what results in periodic motion around the center of magnetic potential well. On the other hand ions experience constantly repulsive force that direct them toward the walls.

The main goal of the thesis is to study the dynamics of trapped electrons using a numerical model and refer theoretical model to experimental evidences.

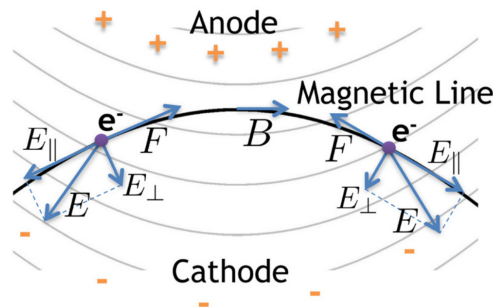


Figure 1: Electric and magnetic field configuration

## 1.2 Electrostatic PIC model

The first and the most important point of the model is that only one charged species will be considered - electrons. So, the collection of particles will not satisfy the condition of quasi-neutrality and is not a real plasma. Strictly speaking, nonneutral or electron plasma is studied in this work.

Because of the rotational symmetry of system, the nonneutral plasma motion can be considered in two dimensions. Two coordinates will be radius  $r$  and the longitudinal  $z$  position in cylindrical coordinates. The region where electron plasma occurs is surrounded from both sides by metallic walls with fixed potentials. Applied magnetic field is not trivial and have complex curvilinear topology. The experimental setup that will be considered throughout this report is schematically described on figure (2).

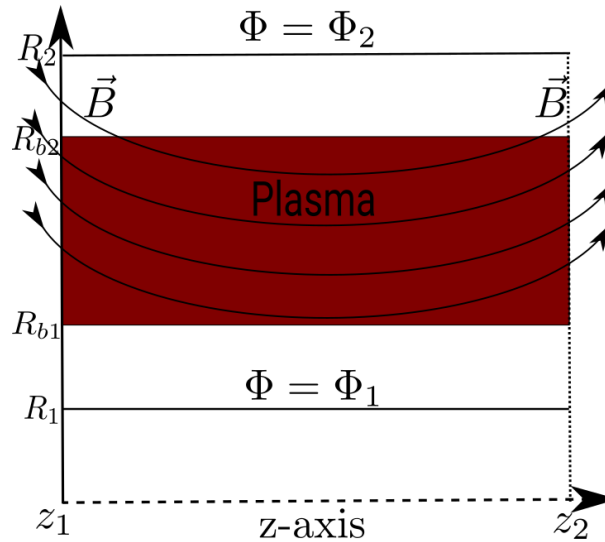


Figure 2: Geometry of the problem

The model applied to further calculation is particle in cell (PIC) method.

Considered equations have the following form:

$$\frac{d\vec{u}}{dt} = \frac{q}{m} \left[ \vec{E}(x, t) + \frac{\vec{u} \times \vec{B}(x)}{\gamma} \right] \quad (1)$$

$$\frac{d\vec{x}}{dt} = \frac{\vec{u}}{\gamma} \quad (2)$$

$$\nabla^2 \phi = -\frac{\rho}{\epsilon_0} \quad (3)$$

where  $\vec{u} = \gamma \vec{v}$ ,  $\gamma = \sqrt{1 + \frac{u^2}{c^2}}$  and  $\vec{x}, \vec{v}$  stand for position and velocity of a particle,  $q, m$  are charge and mass of particle,  $\vec{E}(x, t), \vec{B}(x)$  denote electric and magnetic fields at particle position,  $\rho$  is charge density.

Natural boundary conditions are imposed on two nonneutral plasma edges perpendicular to symmetry axis. Moreover, Dirichlet boundary conditions are imposed on the metallic walls what fully determine solution of the Poisson equation. Hence, boundary conditions take the following mathematical form:

$$\begin{aligned} \phi(R_1, z) &= \phi_1 \\ \phi(R_2, z) &= \phi_2 \\ \frac{\partial \phi(r, z)}{\partial z} \Big|_{z=z_1} &= 0 \\ \frac{\partial \phi(r, z)}{\partial z} \Big|_{z=z_2} &= 0 \end{aligned}$$

Where  $z_1, z_2$  are positions of electron plasma edges, and  $R_1, R_2$  are radii at which metallic walls are placed. The meaning of those parameters is explained on the figure (2).

Momentum and position equations (1), (2) have to be solved for each particle at given time while equation (3) is solved only once for a given time but has to take into account contributions from every single particle.

Important fact is that the electric field  $\vec{E}(x, t)$  is self-consistent. It means that its spatial dependence is determined by positions of all particles. So, electron plasma is pushed by electric field generated by itself. In electrostatic PIC model, only Poisson equation (3) from complete set of Maxwell equations is taken into account. The self-consistent electric field can be expressed then as a gradient of electric potential  $\vec{E}(x, t) = -\vec{\nabla} \phi$ . So, solution of equation (3) with appropriate boundary conditions will be an input to equation (2).

In the model, the magnetic field  $\vec{B}(x)$  is assumed to be time independent and externally imposed. Small effect of moving particle on the magnetic field is negligible with respect to strong external component.

In PIC method, positions and velocities of particles are tracked in continuous phase space, whereas electric and magnetic fields are calculated in the grid points, schematically presented on figure (3). In order to find the magnitudes of the fields in the particle position one has to localize particle in one of the cells and interpolate fields from grid points to exact position.

The mechanism of the calculation is shortly described on figure (3). First of all, the electric field at the grid points is calculated with the equation (3) and interpolated to particle positions. Then, new velocities and positions are calculated according to equations (1) and (2). And those two processes are repeated as long as necessary.

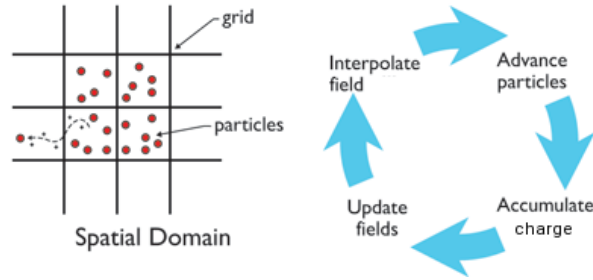


Figure 3: Algorithm of PIC method

### 1.3 Normalization

Equations (1), (2) and (3) define the physical problem to be solved. However, in nonneutral plasma system calculations, very large or very small numbers in standard units are involved. So, it is necessary to prevent the calculation process from possible errors that may come from exceeding the limit of number that can be stored by machine. This is the reason why before implementation above equations have to be turned into form that ensure operation within the optimal range of numbers. Following normalisation constants in which physical quantities will be expressed were considered through all the studies:

$$\begin{aligned}
t_N &= \frac{1}{\omega_{pe}} \\
v_N &= c \\
r_N &= v_N t_N = \frac{c}{\omega_{pe}} \\
B_N &= B_{MAX} \\
E_N &= v_N B_N = c B_{MAX} \\
\phi_N &= E_N r_N = \frac{B_{MAX} c^2}{\omega_{pe}}
\end{aligned}$$

$t_N, v_N, r_N, B_N, E_N, \phi_N$  denotes time, velocity, length, magnetic field, electric field and potential normalisation constants respectively.  $\omega_{pe}$  is electron plasma oscillation frequency defined by elementary constants like elementary charge  $e$ , electron mass  $m_e$ , electric constant  $\epsilon_0$  and electron plasma density  $n_0$  in the following way:  $\omega_{pe} = \sqrt{\frac{n_0 e^2}{m_e \epsilon_0}}$ .  $c$  is the light velocity.  $B_{MAX}$  is the maximal magnitude of external magnetic field. Important fact is that normalisation constant of  $\vec{u}$  is the same as normalisation constant for  $\vec{v}$  because:

$$\vec{u} = \gamma \vec{v} = \gamma v_n \vec{v}' \rightarrow \vec{u}' = \gamma \vec{v}', u_N = v_N$$

Nonneutral plasma consists of large number of electrons of order of magnitude  $10^{20}$ . Simulation of so complex system is impossible if one would like to study each particle separately. Instead of physical particles, numerical superparticles are simulated which are collections of physical neighbouring particles that experience similar forces and their time evolution is also similar. Charge of superparticles is taken such that total charge with respect to original system is conserved. Mass of superparticles is chosen in the way that ratio between charge and mass remains the same as for electron. Mass and charge of superparticles is presented in the following equations:

$$\begin{aligned}
q_{SIM} &= \frac{en_0 V}{N_{SIM}} \\
m_{SIM} &= \frac{q_{SIM} m_e}{e}
\end{aligned}$$

$m_{SIM}, q_{SIM}$  are mass and charge of superparticles,  $e$  is the elementary charge,  $V$  is volume of the space occupied by electrons,  $N_{SIM}$  is the number of superparticles.

Inserting renormalised quantities to equation (1) yields:

$$\begin{aligned}\frac{d\vec{u}}{dt} &= \frac{q}{m} [\vec{E}(x, t) + \frac{\vec{u} \times \vec{B}(x)}{\gamma}] \\ \frac{u_N}{t_N} \frac{d\vec{u}'}{dt'} &= \frac{q_{SIM}}{m_{SIM}} [E_N \vec{E}'(x, t) + u_N B_N \frac{\vec{u}' \times \vec{B}'(x)}{\gamma}] \\ \frac{d\vec{u}'}{dt'} &= \frac{\omega_{ce}}{\omega_{pe}} [\vec{E}'(x, t) + \vec{\beta} \times \vec{B}'(x)]\end{aligned}$$

where  $\vec{\beta} = \frac{\vec{v}}{c}$ . All primes quantities (for example  $v'$ ) are quantities after normalisation.  $\omega_{ce} = \frac{eB_{max}}{m_e}$  is the electron cyclotronic frequency at the maximum of magnitude of magnetic field and is constant. The same process for equation (2) yields:

$$\begin{aligned}\frac{d\vec{x}}{dt} &= \frac{\vec{u}}{\gamma} \\ \frac{r_N}{t_N} \frac{d\vec{x}'}{dt'} &= v_N \frac{\vec{u}'}{\gamma} \\ \frac{d\vec{x}'}{dt'} &= \vec{\beta}\end{aligned}$$

From the equation (3) one get:

$$\begin{aligned}\nabla^2 \phi &= -\frac{\rho}{\epsilon_0} \\ \rho &= -\sum_{p=1}^{N_p} \frac{q_p \delta(r - r_p(t)) \delta(z - z_p(t))}{2\pi r} \\ \nabla^2 \phi' &= -\frac{\omega_{pe}}{\omega_{ce}} \frac{V'}{N_{SIM}} \sum_{p=1}^{N_{SIM}} \frac{\delta(r' - r'_p(t')) \delta(z' - z'_p(t'))}{2\pi r'}\end{aligned}$$

So the final set of equations that will be solved on the machine have the



following form:

$$\frac{d\vec{u}'}{dt'} = \frac{\omega_{ce}}{\omega_{pe}} [\vec{E}'(x, t) + \vec{\beta} \times \vec{B}'(x)] \quad (4)$$

$$\frac{d\vec{x}'}{dt'} = \vec{\beta} \quad (5)$$

$$\nabla^2 \phi' = -\frac{\omega_{pe}}{\omega_{ce}} \frac{V'}{N_{SIM}} \sum_{p=1}^{N_{SIM}} \frac{\delta(r' - r'_p(t')) \delta(z' - z'_p(t'))}{2\pi r'} \quad (6)$$

## 2 Numerical technique

Full set of normalised equations consists of three equations (4),(5) and (6). Each one of them have to be solved with appropriate numerical method described in the following sections.

### 2.1 Poisson equation

In order to solve Poisson equation (6) finite elements method (FEM) was applied. In FEM one introduces discretization mesh and B-spline basis functions that are defined as piecewise polynomials with finite support on considered domain. One has to also specify degree of polynomials. Examples of 1D linear and cubic b-splines are presented on the figure (4). According to the figure (3), Poisson equation has to be solved in two dimensional domain  $r, z$ . It requires introduction of 2D B-splines  $\psi(r, z)$  that are defined through 1D B-splines  $\lambda(r), \phi(z)$  as their product:  $\psi_{i,j}(r, z) = \lambda_i(r) * \phi_j(z)$ . Example of b-spline on 2D domain is presented on the figure (5)

FEM converts original equation (6) into its weak form. In the first step both sides of equation (6) are multiplied by arbitrary test function  $\psi_{i,j}(r, z)$  and integrated over all space  $\int dV = 2\pi \int \int r dr dz$ . In the following computation prime notation for normalized quantities was omitted for simplicity. The weak form of Poisson equation is following:

$$\int \int \vec{\nabla} \phi \vec{\nabla} \psi_{i,j}(r, z) r dr dz - \int_S \psi_{i,j}(r, z) (\vec{n} \cdot \vec{\nabla}) \phi dS = \frac{1}{2\pi} \frac{\omega_{pe}}{\omega_{ce}} \frac{V}{N_{SIM}} \sum_{p=1}^{N_{SIM}} \psi_{i,j}(r_p(t), z_p(t))$$

$\vec{n}$  stands for vector normal to surface  $S$  of integration domain. However, the second term on the left hand side vanishes due to the natural boundary conditions imposed for the electrostatic problem:  $(\vec{n} \cdot \vec{\nabla}) \phi = 0$ . This assumption results in the following weak form of equation (6):

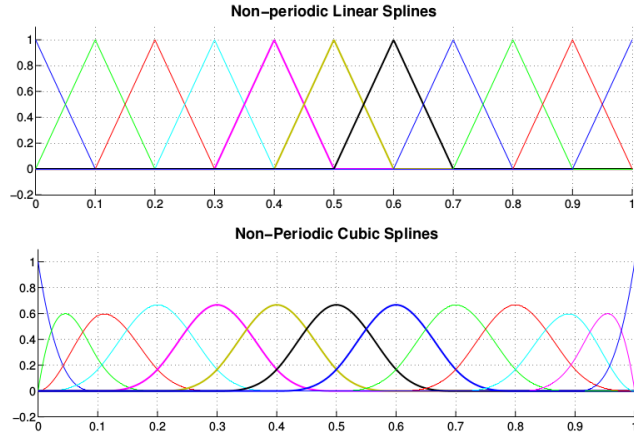


Figure 4: 1D b-spline examples

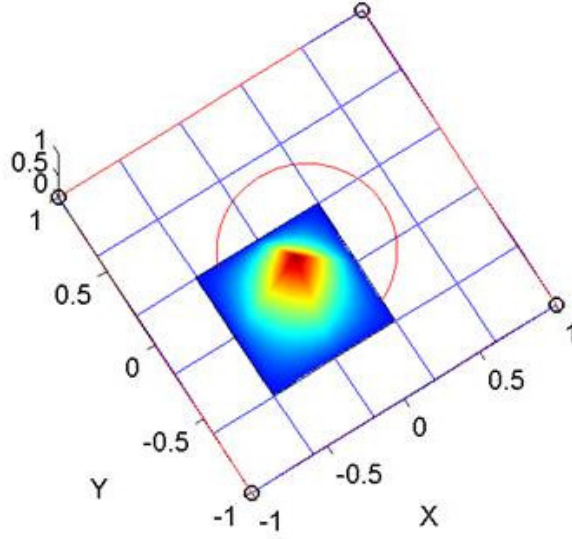


Figure 5: 2D b-spline example

$$\iint \vec{\nabla} \phi \vec{\nabla} \psi_{i,j} r dr dz = \frac{1}{2\pi} \frac{\omega_{pe}}{\omega_{ce}} \frac{V}{N_{SIM}} \sum_{p=1}^{N_{SIM}} \psi_{i,j}(r_p(t), z_p(t)) \quad (7)$$

In order to solve equation (7) numerically it has to be turned into algebraic form. This is done by expansion of potential into series of basis B-splines

functions:  $\phi = \sum_{i'}^{N_r+p} \sum_{j'}^{N_z+p} \phi_{i',j'}(t) \psi_{i',j'}(r, z)$ , where  $N_r + p$  and  $N_z + p$  are numbers of b-splines in radial and z direction respectively. For example, number of b-splines in z direction is given by number of intervals  $N_z$  and order of FEM  $p$ . Inserting this form of potential into equation (7) yields:

$$\sum_{i',j'} \phi_{i',j'}(t) \int \int \vec{\nabla} \psi_{i',j'} \vec{\nabla} \psi_{i,j} r dr dz = \frac{\omega_{pe}}{2\pi\omega_{ce}} \frac{V}{N_{SIM}} \sum_{p=1}^{N_{SIM}} \psi_{i,j}(r_p(t), z_p(t)) \quad (8)$$

Set of equations analogous to equation (8) produced by multiplication of equation (6) by various test functions  $\psi_{i,j}(r, z)$  lead to complex algebraic problem. Mainly, four dimensional arrays are involved which inversion, is very difficult to do. However, those difficulties can be avoided by different numbering of B-splines functions that is presented on the figure (6). Clearly, two indices numbering  $i, j$  is replaced by single indice  $\mu$  such that  $\psi_{i,j}(r, z) \rightarrow \psi_{\mu}(r, z)$  and  $\mu = (j - 1) * (N_z + p) + i$  where  $N_z + p$  is number of b-splines in z direction. Application of new ordering of basis functions yields standard matrix equation (9).

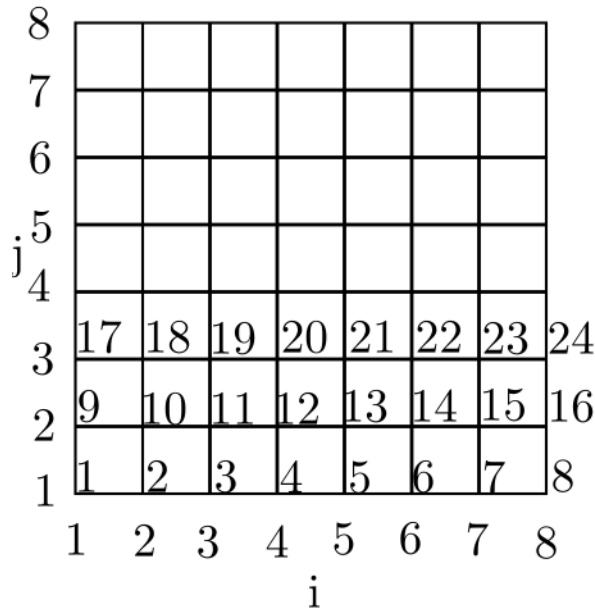


Figure 6: Numbering of basis functions



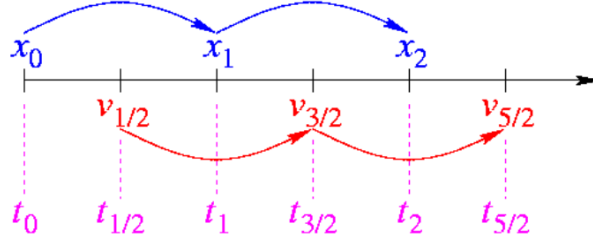


Figure 7: Leapfrog scheme

$$\frac{\vec{u}_{n+\frac{1}{2}} - \vec{u}_{n-\frac{1}{2}}}{\Delta t} = \frac{\omega_{ce}}{\omega_{pe}} [\vec{E}(x_n, t) + \frac{\vec{u}_{n+\frac{1}{2}} + \vec{u}_{n-\frac{1}{2}}}{2\gamma_n} \times \vec{B}(x_n)] \quad (11)$$

$$\frac{\vec{x}_{n+1} - \vec{x}_n}{\Delta t} = \frac{\vec{u}_{n+\frac{1}{2}}}{\gamma_{n+\frac{1}{2}}} \quad (12)$$

Let's assume the positions of particles  $x_n$  at time  $t_n$  and particles velocities  $v_{n-\frac{1}{2}}$  at time  $t_{n-\frac{1}{2}}$  are known. Then, one can calculate electric field from particles positions from equation (9) to advance velocity in time. Updated velocities are used to move particles to new positions which define new electric field and so on. So, the process may be continued as long as it is necessary.

In order to solve equation (11) Boris method [1] was used. The method substitutes original velocities  $\vec{u}_{n+\frac{1}{2}}$  and  $\vec{u}_{n-\frac{1}{2}}$  by:

$$\vec{u}_{n-\frac{1}{2}} = \vec{u}^- - \frac{\omega_{ce}}{\omega_{pe}} \frac{\vec{E}(x_n, t) \Delta t}{2} \quad (13)$$

$$\vec{u}_{n+\frac{1}{2}} = \vec{u}^+ + \frac{\omega_{ce}}{\omega_{pe}} \frac{\vec{E}(x_n, t) \Delta t}{2} \quad (14)$$

Inserting new velocities to equation (11) yields:

$$\frac{\vec{u}^+ - \vec{u}^-}{\Delta t} = \frac{\omega_{ce}}{\omega_{pe}} \left( \frac{\vec{u}^+ + \vec{u}^-}{2\gamma_n} \right) \times \vec{B}(x_n) \quad (15)$$

Equation (15) is pure rotation around electric field line of new velocities. Summing up, Boris method consists of three consecutive steps in integration of momentum equation:

- Addition of half of electric pulse  $\frac{\omega_{ce}}{\omega_{pe}} \frac{\vec{E}(x_n, t) \Delta t}{2}$  to initial velocity  $\vec{u}_{n-\frac{1}{2}}$  in order to calculate  $\vec{u}^-$  and update of  $\gamma_{n-\frac{1}{2}}$  to  $\gamma_n = \sqrt{1 + (\frac{u^-}{c})^2}$ .
- Rotation around magnetic field yields  $\vec{u}^+$ . Note that  $\gamma_n$  remains constant during the rotation, as the magnetic field does not work.
- Addition of second half of electric pulse  $\frac{\omega_{ce}}{\omega_{pe}} \frac{\vec{E}(x_n, t) \Delta t}{2}$  to  $\vec{u}^+$  in order to get  $\vec{u}_{n+\frac{1}{2}}$ .

The last remaining issue is the way how rotation is performed. According to [1], it is convenient to introduce a vector  $\vec{u}'$  which is perpendicular to both magnetic field  $\vec{B}$  and velocity increment  $\vec{u}^+ - \vec{u}^-$ :

$$\vec{u}' = \vec{u}^- + \vec{u}^- \times \vec{t} \quad (16)$$

Where  $\vec{t} = \frac{\omega_{ce}}{\omega_{pe}} \frac{\vec{B} \Delta t}{2\gamma_n}$ . Finally,  $\vec{u}^+ - \vec{u}^-$  is parallel to  $\vec{u}^- \times \vec{B}$ , so

$$\vec{u}^+ = \vec{u}^- + \vec{u}' \times \vec{s} \quad (17)$$

where  $\vec{s}$  is parallel to  $\vec{B}$  and its magnitude is determined by the requirement  $|\vec{u}^-|^2 = |\vec{u}^+|^2$ :

$$\vec{s} = \frac{2\vec{t}}{1 + t^2} \quad (18)$$

The geometry of the problem is schematically presented on the figure (8).

### 2.2.2 Details of calculations

Equations derived in the previous section are given in correct form from mathematical point of view. However, in order to implement considered equations in programming language one has to derive analogous formulas for each one of three components. Momentum equations are solved in cylindrical coordinates in the way described in this section.

It is assumed that initial positions of particles  $x_n$  and initial velocities  $v_{n-\frac{1}{2}}$  are given. So that, electric field can be calculated by solving Poisson equation (9). During acceleration, particles remain at the same positions and then they are moved by updated velocity. So, reference frame does not change at the first step where only particles velocities change.

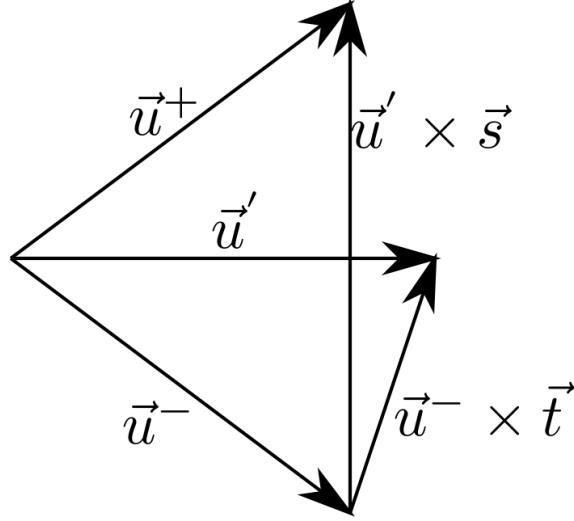


Figure 8: Rotation around magnetic field

First of all, half of electric pulse is added to initial velocity  $v_{n-\frac{1}{2}}$  in order to calculate  $\vec{u}^-$  from equation (13). In the following computations the notation  $\tau = \frac{\omega_{ce}\Delta t}{2\omega_{pe}}$  is chosen for clarity:

$$\begin{aligned} \vec{u}^- &= \vec{u}_{n-\frac{1}{2}} + \tau \vec{E}(x_n, t) \\ \begin{bmatrix} u_r^- \\ u_\theta^- \\ u_z^- \end{bmatrix} &= \begin{bmatrix} u_{n-\frac{1}{2},r} + \tau E_r(x_n, t) \\ u_{n-\frac{1}{2},\theta} \\ u_{n-\frac{1}{2},z} + \tau E_z(x_n, t) \end{bmatrix} \end{aligned} \quad (19)$$

Subscripts  $r, \theta, z$  denote respective components of considered values in cylindrical coordinates. In equation (19), it was taken into account that one component of electrical field  $E_\theta$  is equal to zero due to the symmetry. The same assumption is done on the external magnetic field configuration such that  $\vec{B}(x_n) = [B_r(x_n) \ B_z(x_n) \ 0]$ . Then,  $\gamma_n$  is recalculated in the following way:  $\gamma_n = \sqrt{1 + (\frac{u^-}{c})^2}$

After the first half of the acceleration due to the electric field, rotation around magnetic field is performed. At first, it is convenient to calculate  $\vec{u}'$

in the way demonstrated in the equation (16):

$$\begin{aligned} \vec{u}' &= \vec{u}^- + \vec{u}^- \times \vec{t} \\ \begin{bmatrix} u_r' \\ u_\theta' \\ u_z' \end{bmatrix} &= \begin{bmatrix} u_r^- + \frac{\tau}{\gamma_n} u_\theta^- B_z(x_n) \\ u_\theta^- + \frac{\tau}{\gamma_n} (u_z^- B_r(x_n) - u_r^- B_z(x_n)) \\ u_z^- - \frac{\tau}{\gamma_n} u_\theta^- B_r(x_n) \end{bmatrix} \end{aligned} \quad (20)$$

Following identities between units vectors  $\vec{e}_r, \vec{e}_z, \vec{e}_\theta$  were used in the calculations:

$$\begin{aligned} \vec{e}_r \times \vec{e}_z &= -\vec{e}_\theta \\ \vec{e}_\theta \times \vec{e}_z &= \vec{e}_r \\ \vec{e}_r \times \vec{e}_\theta &= \vec{e}_z \end{aligned}$$

Then, results of equations (19) and (20) are used in order to calculate  $\vec{u}^+$ . According to equation (17):

$$\begin{aligned} \vec{u}^+ &= \vec{u}^- + \vec{u}' \times \vec{s} \\ \begin{bmatrix} u_r^+ \\ u_\theta^+ \\ u_z^+ \end{bmatrix} &= \begin{bmatrix} u_r^- + \frac{\Omega}{\gamma_n} u_\theta' B_z(x_n) \\ u_\theta^- + \frac{\Omega}{\gamma_n} (u_z' B_r(x_n) - u_r' B_z(x_n)) \\ u_z^- - \frac{\Omega}{\gamma_n} u_\theta' B_r(x_n) \end{bmatrix} \end{aligned} \quad (21)$$

Where  $t^2 = (\frac{\tau}{\gamma_n})^2 |\vec{B}(x_n)|^2$  and  $\Omega = \frac{2\tau}{1+t^2}$ . In the last step, second half of electric pulse is added to  $\vec{u}^+$  calculated in equation (21) in the same way as it was done in equation (19):

$$\begin{aligned} \vec{u}_{n+\frac{1}{2}} &= u^+ + \tau \vec{E}(x_n, t) \\ \begin{bmatrix} u_{n+\frac{1}{2},r} \\ u_{n+\frac{1}{2},z} \\ u_{n+\frac{1}{2},\theta} \end{bmatrix} &= \begin{bmatrix} u_r^+ + \tau E_r(x_n, t) \\ u_z^+ + \tau E_z(x_n, t) \\ u_\theta^+ \end{bmatrix} \end{aligned} \quad (22)$$

When velocity  $v_{n+\frac{1}{2}}$  is calculated, one can advance positions of particles from  $x_n$  to  $x_{n+1}$ . However, some difficulties arise from the fact that cylindrical coordinates are used and unit vectors are not fixed at time but move together with the particle.



In Cartesian coordinates solution of equation (12) leads to:

$$x_{n+1} = x_n + \frac{u_{n+\frac{1}{2},x}}{\gamma_{n+\frac{1}{2}}} \Delta t \quad (23)$$

$$y_{n+1} = y_n + \frac{u_{n+\frac{1}{2},y}}{\gamma_{n+\frac{1}{2}}} \Delta t \quad (24)$$

$$z_{n+1} = z_n + \frac{u_{n+\frac{1}{2},z}}{\gamma_{n+\frac{1}{2}}} \Delta t \quad (25)$$

Where  $x, y, z$  denote respective coordinates in the Cartesian reference frame. Let the z-axis of cylindrical reference frame overlap the z-axis of Cartesian reference frame. Then, z component of total position is calculated in the same way in both reference frames by equation (25). But remaining two components at the plane perpendicular to z-axis are differently calculated in cylindrical and Cartesian reference frames.

Assuming that initial radius and angle ( $r_n$  and  $\theta_n$ ) are given, one introduces a reference frame  $x'y'$  such that  $x'$  axis point along radial direction and  $y'$  axis point in  $\theta$  direction. Then, particles are moving in  $x'y'$  reference frame in the way described in equations (23) and (24):

$$x_{n+1} = r_n + \frac{u_{n+\frac{1}{2},r}}{\gamma_{n+\frac{1}{2}}} \Delta t \quad (26)$$

$$y_{n+1} = \frac{u_{n+\frac{1}{2},\theta}}{\gamma_{n+\frac{1}{2}}} \Delta t \quad (27)$$

Then, coordinates of advanced particles are converted to new radius  $r_{n+1}$  and angle  $\theta_{n+1}$  at updated cylindrical reference frame:

$$r_{n+1} = \sqrt{x_{n+1}^2 + y_{n+1}^2} \quad (28)$$

$$\theta_{n+1} = \theta_n + \alpha \quad (29)$$

$$\alpha = \arctan \frac{y_{n+1}}{x_{n+1}} \quad (30)$$

The geometrical interpretation of the performed calculations when particles are moving are presented on the figure (9).

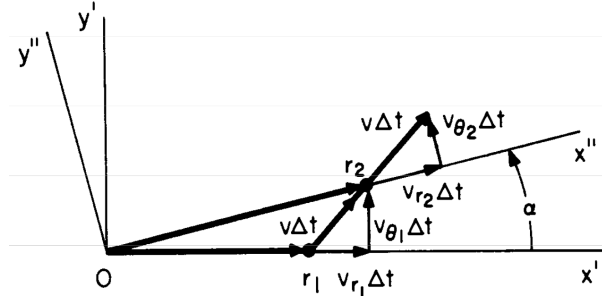


Figure 9: Plane perpendicular to z-axis [1]

According to the figure (9), advancing the particles involve rotation of the reference frame. So, it is required to compute components of velocity  $v_n$  in new reference frame through rotation by angle  $\alpha$ :

$$\begin{bmatrix} v_{n+\frac{1}{2},r} \\ v_{n+\frac{1}{2},\theta} \end{bmatrix}_{x''y''} = \begin{bmatrix} \cos \alpha & \sin \alpha \\ -\sin \alpha & \cos \alpha \end{bmatrix} \begin{bmatrix} v_{n+\frac{1}{2},r} \\ v_{n+\frac{1}{2},\theta} \end{bmatrix}_{x'y'} \quad (31)$$

Where  $\sin \alpha = \frac{y_{n+1}}{r_{n+1}}$  and  $\cos \alpha = \frac{x_{n+1}}{r_{n+1}}$ .

## 3 Implementation

### 3.1 Initialization

First of all it is necessary to describe initial positions and velocities of electrons. The most intuitive initial state is random distribution along both  $z$  and  $r$  direction presented schematically on the figure (12). But this configuration does not fill the space uniformly like it would be expected. There are empty parts of the space and some with high concentration of particles.

Moreover, according to [1] using usual random initialization tends to produce computed nonneutral plasmas with undesired fluctuation levels which are larger than fluctuations observed in laboratory. This may prevent us from observing low level physics. The solution is to load initial phase space as smoothly as possible but still resembling random configuration of particles. The method is called quite start. Particles are distributed uniformly with respect to the first coordinate such that:  $z_i = \frac{i+\frac{1}{2}}{N}L_z$ , where  $i = 0, \dots, N-1$ ,  $N$  is total number of particles and  $L_z$  is the length of the cylinder. The second

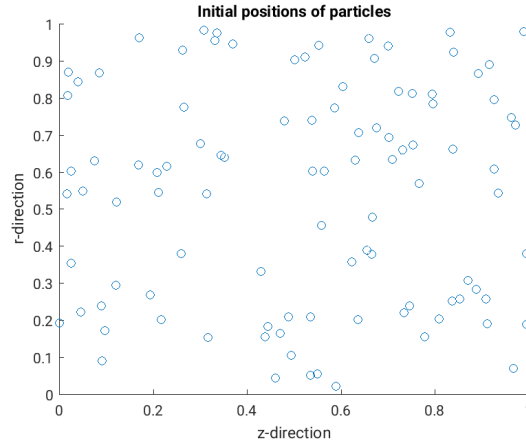


Figure 10: Initial random positions

coordinate is loaded as a Hammersley sequence that consists of bit reversed numbers. The sequence is constructed by reversing the base-n representation of the sequence of natural numbers. Two examples of base 2 and 3 Hammersley sequences are given in the table (1). Resulting configuration of initial positions of particles with a base-2 Hammersley sequence is presented on the figure (11).

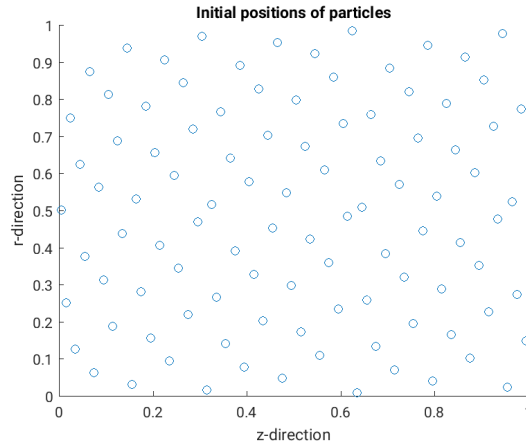


Figure 11: Initial position of particles with a base-2 Hammersley sequence

Particles velocities can be initialised in several ways. For electron plasmas with relatively low temperature, cold plasma approximation can be applied.

Natural number	Base-2 repr.	Base-2 Hammerslay sequence	Base-3 repr.	Base-3 Hammerslay sequence
0	0	0	0	0
1	1	$1 * \frac{1}{2} = \frac{1}{2}$	1	$1 * \frac{1}{3} = \frac{1}{3}$
2	10	$1 * \frac{1}{4} + 0 * \frac{1}{2} = \frac{1}{4}$	2	$2 * \frac{1}{3} = \frac{2}{3}$
3	11	$1 * \frac{1}{4} + 1 * \frac{1}{2} = \frac{3}{4}$	10	$1 * \frac{1}{9} + 0 * \frac{1}{3} = \frac{1}{9}$
4	100	$1 * \frac{1}{8} + 0 * \frac{1}{4} + 0 * \frac{1}{2} = \frac{1}{8}$	11	$1 * \frac{1}{9} + 1 * \frac{1}{3} = \frac{4}{9}$
5	101	$1 * \frac{1}{8} + 0 * \frac{1}{4} + 1 * \frac{1}{2} = \frac{5}{8}$	12	$1 * \frac{1}{9} + 2 * \frac{1}{3} = \frac{7}{9}$
6	110	$1 * \frac{1}{8} + 1 * \frac{1}{4} + 0 * \frac{1}{2} = \frac{3}{8}$	20	$2 * \frac{1}{9} + 0 * \frac{1}{3} = \frac{2}{9}$
7	111	$1 * \frac{1}{8} + 1 * \frac{1}{4} + 1 * \frac{1}{2} = \frac{7}{8}$	21	$2 * \frac{1}{9} + 1 * \frac{1}{3} = \frac{5}{9}$

Table 1: Hammerslay sequence examples

It simply means, that initial velocities of electrons are equal to zero.

At higher temperatures, gaussian distribution of velocities is a better choice. In order to reproduce gaussian distribution function, cumulative distribution function is introduced:

$$F(v) = \frac{\int_0^v \exp -\frac{v^2}{2v_t^2} dv}{\int_0^\infty \exp -\frac{v^2}{2v_t^2} dv} \quad (32)$$

Function  $F(v)$  ranges between 0 and 1. There is a well defined velocity for each number from 0 to 1. So, by a good choice of set of numbers it is possible to correctly initialize particles velocities. Again, a random set of numbers will lead to a different distribution. However, it turns out that 'quite Maxwellian' with set of numbers defined by Hammerslay sequence give desired result. Histogram of velocities in 1D is shown on the figure (12).

### 3.2 Poisson equation solver

According to the equation (9), positions of the particles are involved in derivation of potential generated by themselves. Right hand side of the equation is called charge assignment and describe charge deposited on the grid points. It has one important property that can be used as a test for the code:

$$\sum_i Q_i(t) = \frac{1}{2\pi} \frac{\omega_{pe}}{\omega_{ce}} \frac{V}{N_{SIM}} \sum_{p=1}^{N_{SIM}} \sum_i \psi_i(r_p(t), z_p(t)) = \frac{1}{2\pi} \frac{\omega_{pe}}{\omega_{ce}} V \quad (33)$$

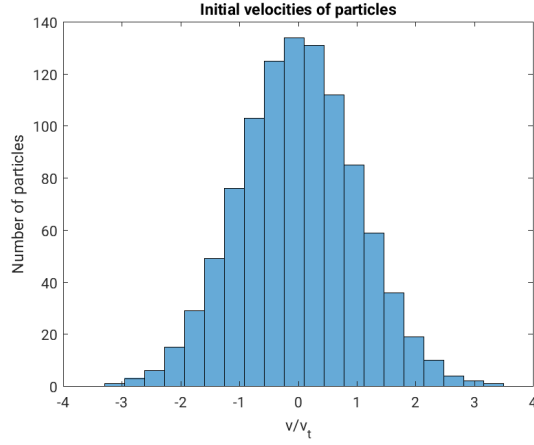


Figure 12: Histogram of velocities in 1D

So, the sum of elements of right hand side vector should be fully determined by number of superparticles and constant factor  $\frac{1}{2\pi} \frac{\omega_{pe}}{\omega_{ce}} V$ . The difference between sum of components of numerically calculated right hand side and equation (33) was measured for the range of number of superparticles between 10 and  $10^7$  and its result is presented on the figure (13).

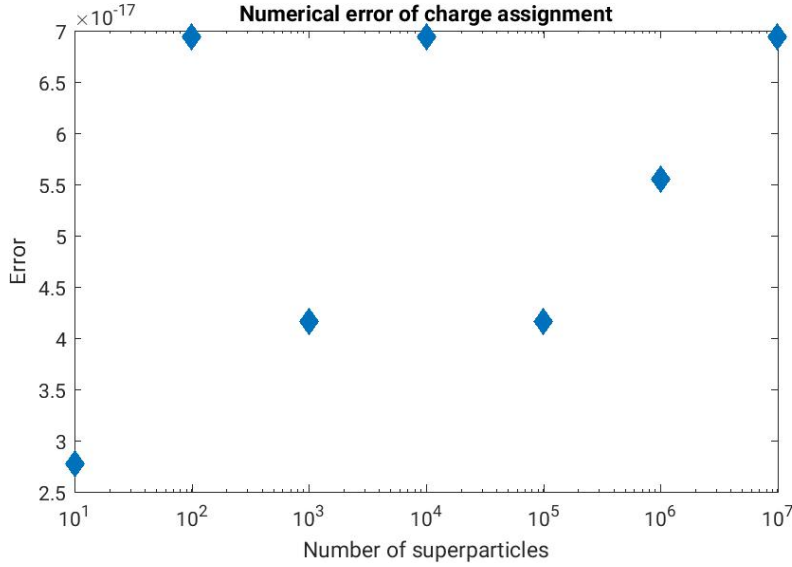


Figure 13: Error of charge assignment

The error is of the order of magnitude of machine precision which is equal to  $10^{-17}$ . Once it was checked that right hand side of equation (9) is assembled correctly, it is necessary to perform tests on entire poisson equation solver. The tests are done for cases where the potential can be calculated analytically.

### 3.2.1 Case of empty space between metallic walls

In the first test it is assumed that there is no particles in the space between metallic walls with fixed potential (figure (2)). The geometry corresponds to a simple cylindrical capacitor schematically presented on the figure (14).

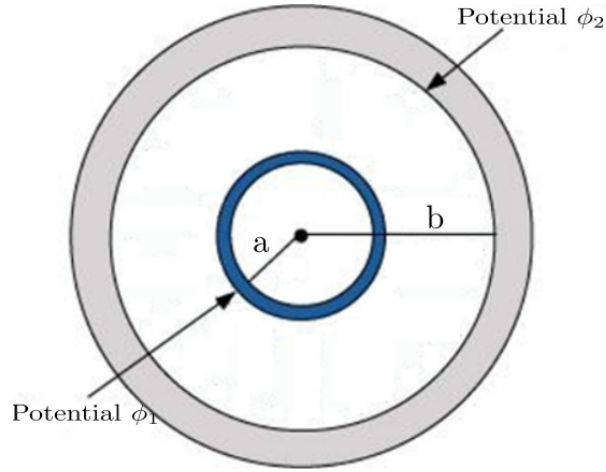


Figure 14: Cross-section at plane perpendicular to  $z$ -axis of cylindrical capacitor

Parameters used in the calculations are shown in the table (2)

a	b	$L_z$	$V(a)$	$V(b)$	$n_0$
0.05 m	0.06 m	0.07 m	0 V	30 000 V	$0m^{-3}$

Table 2: Parameters

The considered system is highly symmetric. First of all there is a symmetry with respect to the angle. Moreover, if length of the cylinder is large enough it can be assumed that there is also symmetry along the main axis. So, all quantities are only radial dependent.

Analytical solution for potential is derived from Laplace equation with appropriate boundary conditions. 1D problem to be solved has the following form:

$$\begin{aligned}\frac{1}{r} \frac{d}{dr} r \frac{d}{dr} \phi &= 0 \\ \phi|_{r=a} &= \phi_1 \\ \phi|_{r=b} &= \phi_2\end{aligned}\tag{34}$$

The problem is a second order ordinary differential equation with two boundary conditions. So, a unique solution exists and is derived in the following way:

$$\begin{aligned}\frac{1}{r} \frac{d}{dr} r \frac{d}{dr} \phi &= 0 \\ \frac{d}{dr} r \frac{d}{dr} \phi &= 0 \\ \frac{d}{dr} \phi &= \frac{C_1}{r} \\ \int_{\phi_1}^{\phi(r)} d\phi &= \int_a^r \frac{C_1}{r} dr \\ \phi(r) &= \phi_1 + C_1 \ln\left(\frac{r}{a}\right)\end{aligned}$$

In order to calculate the integration constant  $C_1$  second boundary condition is applied:

$$\phi(r=b) = \phi_1 + C_1 \ln\left(\frac{b}{a}\right) = \phi_2 \rightarrow C_1 = \frac{\phi_2 - \phi_1}{\ln\left(\frac{b}{a}\right)}$$

So, the final solution has the form presented in the equation (35).

$$\phi(r) = \phi_1 + \frac{\phi_2 - \phi_1}{\ln\left(\frac{b}{a}\right)} \ln\left(\frac{r}{a}\right)\tag{35}$$

Derived analytical solution is compared with the one obtained numerically on the figure (15).

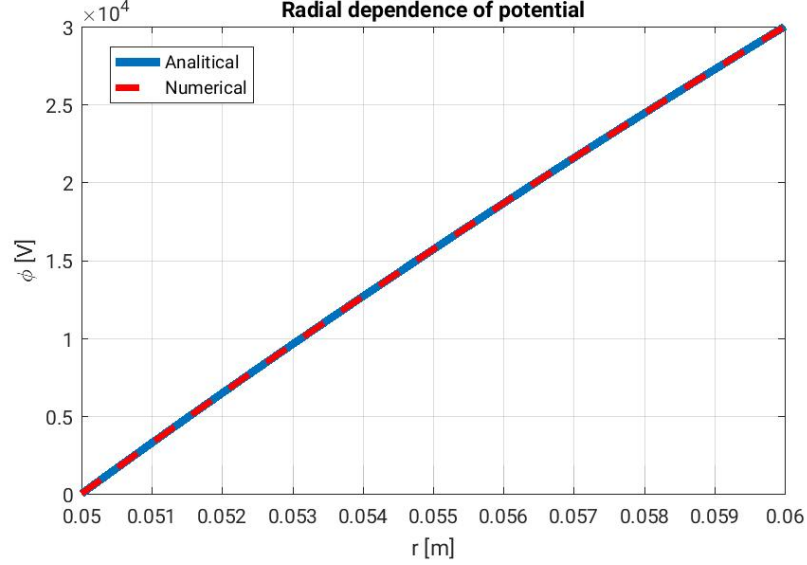


Figure 15: Radial dependence of potential

So, the numerical solution  $\phi_{num}$  matches perfectly the analytical  $\phi_{anal}$  one in this simple example. However, the error analysis was performed in order to check if error converge to zero if discretisation becomes more and more accurate. First of all, profiles of differences between numerical and analytical solutions were studied for different numbers of intervals for discretization (figure(16)).

According to the figure (16), it is evident that difference between two solutions becomes smaller with increasing number of intervals  $n_r$ . It still has to be investigated if the error between two solutions tends to zero when number of cells tends to infinity. First of all, error was defined as an infinite norm that can be approximated as a maximal difference between two solutions in grid points:

$$err(\phi_{anal}, \phi_{num}) = \|\phi_{anal}(r) - \phi_{num}(r)\|_{\infty} \approx \max_{i=1 \dots n_r+1} |\phi_{anal}(r_i) - \phi_{num}(r_i)|$$

Convergence of error was studied for the first up to fourth order of finite elements method. Results are presented on figure (17).

Error between numerical and analytical solution tend to zero independently on the order of finite elements method. Moreover, it was proven that



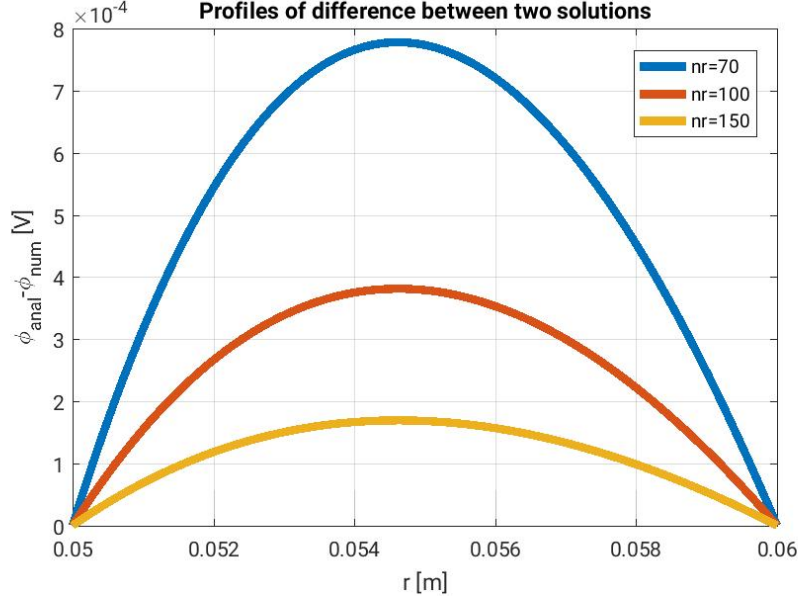


Figure 16: Difference between analytical and numerical solutions

error behave like  $(1/n_r)^{p+1}$  where  $p$  is the order of the finite elements method. Exception is second order finite elements method where convergence is one order higher than expected. This discrepancy may come from the estimation of error where the norm was taken only at the grid points. But as long as the numerical method converge to analytical one it can be assumed that solver has been implemented properly.

Based on this example one can conclude that the left hand side of equation (9) is constructed correctly because the right hand side does not play a role in this case.

Now, when both right and left side of poisson equation solver was tested separately, one can add complexity into the setup by adding a electron plasma.

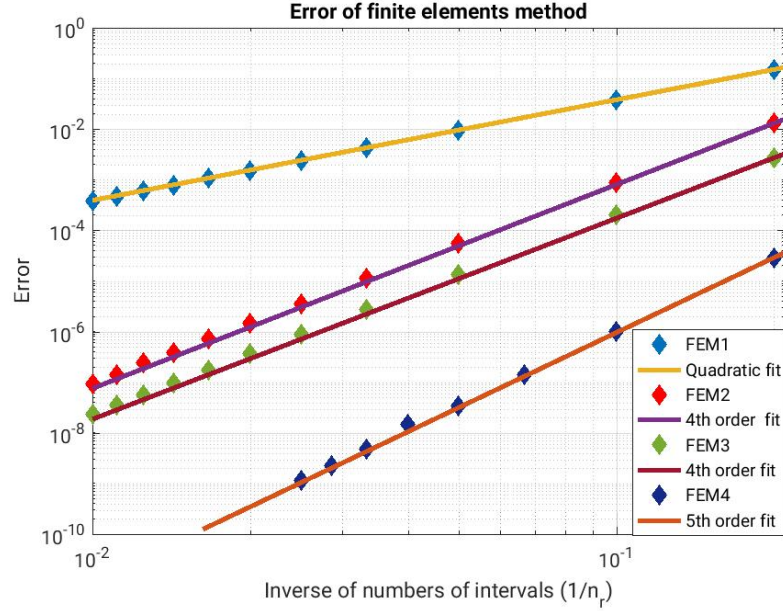


Figure 17: Difference between analytical and numerical solutions

### 3.2.2 Thin layer of electron plasma

The next example introduces some complexity with respect to the previous section. Very thin cylindrical layer of electron plasma is considered inside a space limited by two metallic walls. It is assumed that all electrons form a homogeneous layer compressed to one interval of discretisation scheme. So, increasing the number of intervals will make the layer thinner and thinner.

The system remains symmetric with respect to  $z$  and  $\theta$  for the same reason as in the previous section. Problem to be solved is described by Poisson equation with appropriate boundary conditions:

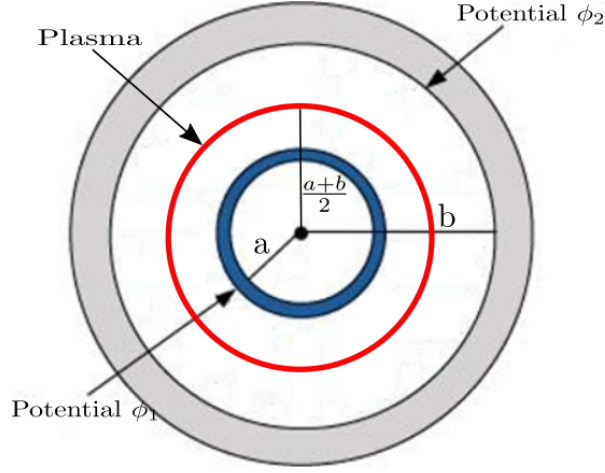


Figure 18: Cross-section at plane perpendicular to z-axis of cylindrical capacitor

$$\frac{1}{r} \frac{d}{dr} r \frac{d}{dr} \phi = -\frac{\rho}{\epsilon_0} \quad (36)$$

$$\rho = \begin{cases} \rho_0 & \text{if } R_{b1} < r < R_{b2} \\ 0 & \text{otherwise} \end{cases} \quad (37)$$

$$\phi|_{r=a} = \phi_1$$

$$\phi|_{r=b} = \phi_2$$

Where  $\rho$  is the electron plasma density which is constant at one middle interval and is zero otherwise. Boundary values of potential and geometrical parameters were taken from table (2). Analytical solution of the problem with finite width of nonneutral plasma was derived by solving equation (36) and compared with numerical one on the figure (19).

Again, both solutions match each other. The difference between them decreases when the number of points for the discretization is increased, as can be seen on figure (20). Error analysis was performed for the first up to fourth order finite elements method and is shown on the figure (21). Order of convergence for the first order FEM is quadratic like it is expected. However, order of convergence for higher order FEM is underestimated by 1,2,4 for second, third and fourth order FEM respectively. The reason for this discrepancy may come from the fact that at higher order finite elements

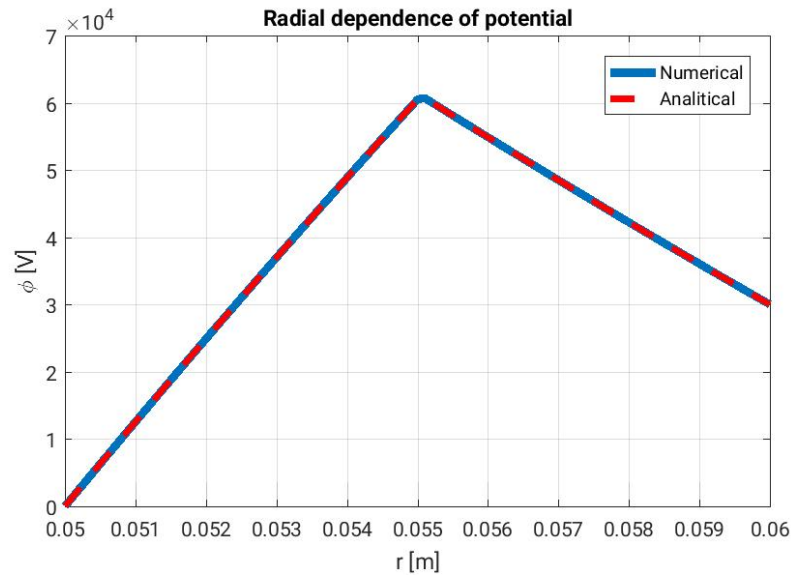


Figure 19: Radial dependence of potential

some charges are assigned to grid points that are not the limits of interval at which particles are placed.

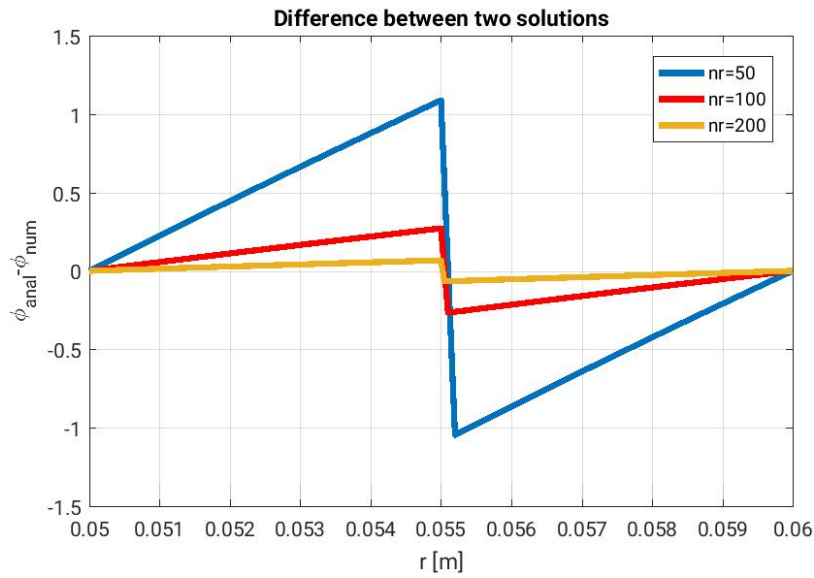


Figure 20: Difference between analytical and numerical solutions for FEM of the first order

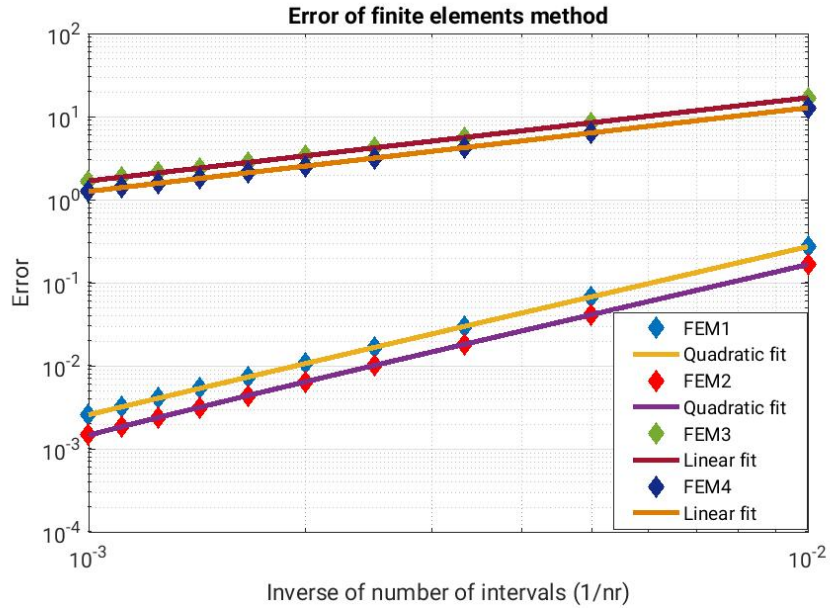


Figure 21: Error of FEM of the first order

## 4 Particles mover

### 4.1 Magnetic field topology

So far, only the Poisson equation, from the full set of equations (1), (2) and (3) was tested. Now it is known that for a given distribution of charge the self-consistent potential is calculated correctly. However, particles are pushed by both electric and magnetic fields. The magnetic field is assumed to be given externally by surrounding coils in the analytic form [2]. The mirror magnetic potential is described by the following formula:

$$A_\theta^{ext} = \frac{B_0}{2} \left[ r - \frac{L}{\pi} \frac{R-1}{R+1} I_1\left(\frac{2\pi r}{L}\right) \cos\left(\frac{2\pi z}{L}\right) \right] \quad (38)$$

So only one component of vectorial potential is not vanishing. In equation (38),  $I_1(x)$  is the modified Bessel function of the first order of the first kind.  $L$  is the distance between magnetic mirrors (located at  $z = \pm \frac{L}{2}$ ).  $B_0$  is the value of the axial magnetic field on the axis at  $z = \pm \frac{L}{4}$ .  $R$  is the mirror ratio defined as  $R = \frac{B_{max}}{B_{min}} = \frac{B(r=0, z=\pm \frac{L}{2})}{B(r=0, z=0)}$ . So, by manipulating two parameters  $B_0$  and  $R$  one can modify the magnitude and the shape of magnetic field lines. Resulting magnetic field has two nonvanishing components:

$$B_r^{ext}(r, z) = -\frac{\partial}{\partial z} A_\theta^{ext}(r, z) = -B_0 \frac{R-1}{R+1} I_1\left(\frac{2\pi r}{L}\right) \sin\left(\frac{2\pi z}{L}\right) \quad (39)$$

$$B_z^{ext}(r, z) = \frac{1}{r} \frac{\partial}{\partial r} [r A_\theta^{ext}(r, z)] = B_0 \left[ 1 - \frac{R-1}{R+1} I_0\left(\frac{2\pi r}{L}\right) \cos\left(\frac{2\pi z}{L}\right) \right] \quad (40)$$

Magnetic field flux through the circle of radius  $r$  is derived from vectorial potential:

$$\Phi_B = \int_S \vec{B} \cdot d\vec{S} = \int_{\delta S} \vec{A} \cdot d\vec{l} = \int_0^{2\pi} A_\theta r d\theta = 2\pi r A_\theta \quad (41)$$

Magnetic flux from equation (41) is drawn on the figure (22). Magnetic field lines are isolines of magnetic flux from figure (22). Magnetic field lines are presented on figure (23). Parameters specific to the magnetic field are presented in table (3). As the guiding center of particles follow magnetic field lines, one should avoid the intersections of magnetic field lines at which particles are initialized with metallic walls. In order to avoid particles hitting the walls one has to also take into account gyromotion of particles. So, all the magnetic field lines which are followed by particles should not be closer than a distance of Larmor radius from metallic walls.

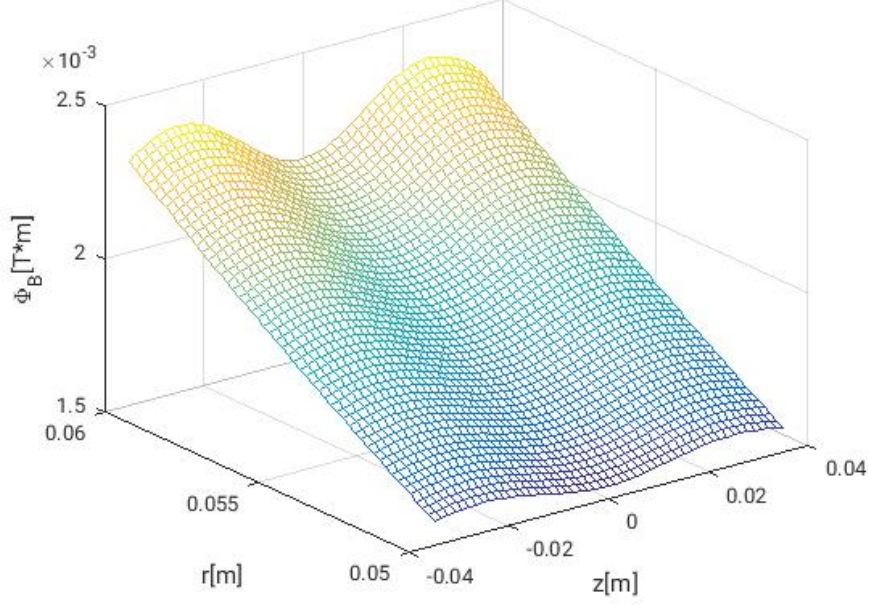


Figure 22: Magnetic flux

Table 3: Magnetic field parameters

$B_0$	$R$	$L$
0.2T	1.001	0.05m

## 4.2 Mirror effect

The magnetic field configuration presented in the previous section is an example of magnetic mirror. In a magnetic mirror, electromagnets are used to produce increasing density of magnetic field lines at both ends of device (figure (24)). Trapped particles experience repulsive force which push them to the confinement area with low magnetic field. Confinement is efficient only if particle do not belong to a loss cone, defined by the ratio between their perpendicular and parallel velocities. The condition for particle to be confined is expressed in the following way:

$$\frac{v_{\perp}}{v_{\parallel}} > \sqrt{\frac{B_{min}}{B_{max}}} \quad (42)$$

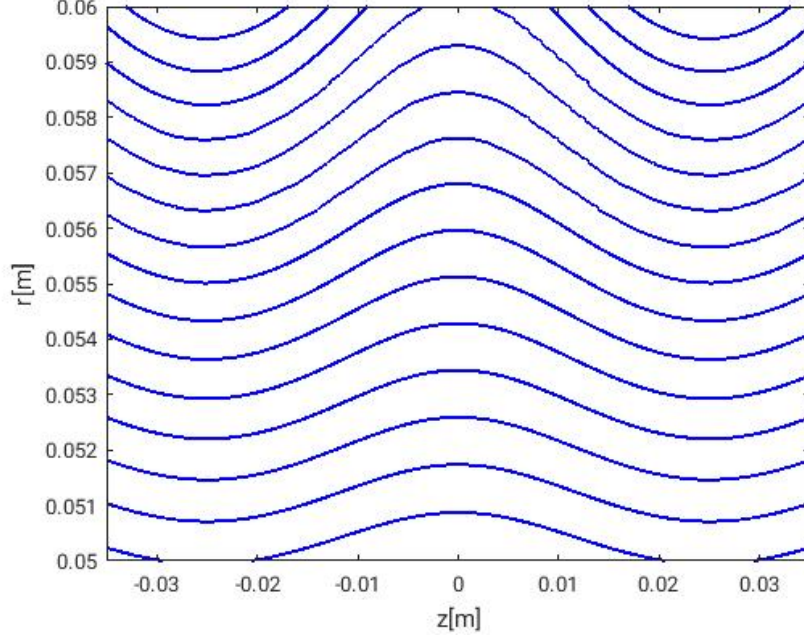


Figure 23: Magnetic field lines

So, the ratio between perpendicular and parallel velocity of particle must be high enough to confine the particles. Two effects should be noticed while studying single particle trajectory:

- Particle should follow the magnetic field line at which it is initially placed
- Particle with too slow gyromotion with respect to the movement along field lines will not be trapped

For this example where single particle is considered, the potential is determined externally by boundary conditions (no self-consistent component). According to the table (4), there is no difference of potential between the two metallic walls, so the particle experience only magnetic field. At first, single particle trajectory was studied for the ratio  $\frac{v_{\perp}}{v_{\parallel}} = 2$  ( $v_{\perp} = 0.02c$  and  $v_{\parallel} = 0.01c$ ) and reflection from strong magnetic field area was expected. On the other hand, the particle with dominant parallel velocity  $\frac{v_{\perp}}{v_{\parallel}} = \frac{1}{2}$  and ( $v_{\perp} = 0.005c$  and  $v_{\parallel} = 0.01c$ ) should pass the area of high magnetig field.



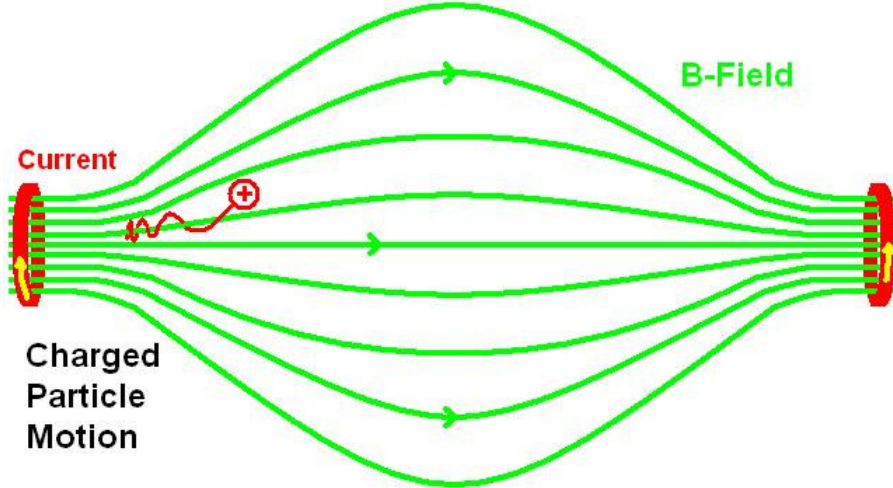


Figure 24: Magnetic mirror

The trajectories of those particles are presented on figure (25). According to the figure (25) particles follow magnetic field lines as expected. Moreover, the theoretical condition for magnetic confinement is verified. Numerical and physical parameters used in the calculation of particle trajectories are shown in the table (4). The dimensions of the cylinder remains the same and are indicated in the table (2).

Table 4: Input parameters

$\Phi_1$	$\Phi_2$	$B_0$	$R$	$dt$	$n_{steps}$	$Q_{SIM}$
0V	0V	0.2T	1.003	$10^{-12}s$	$10^4$	$-1.55 \cdot 10^{-17}C$

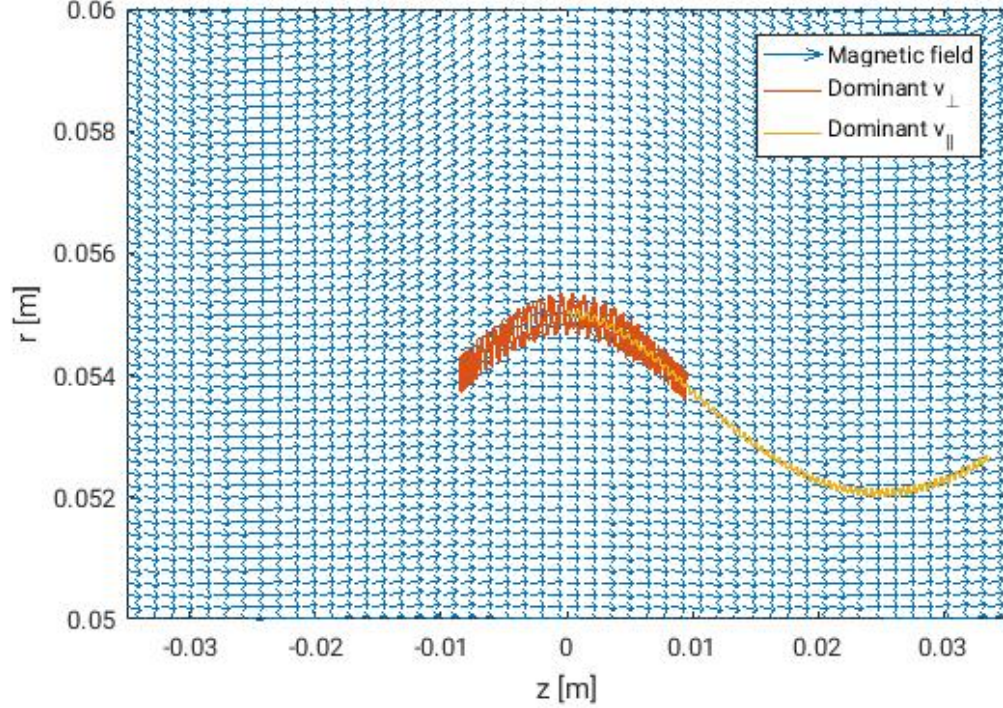


Figure 25: Trajectory of particle with dominant perpendicular and parallel velocity

### 4.3 Penning mechanism

In the previous example particles were confined only by the mirror magnetic field configuration. However, there also exists a mechanism of trapping the particles by appropriate configuration of both electric and magnetic field. This mechanism is presented and experimentally studied by Pagonakis et al. [3]. Penning trapping takes place if equipotential lines intersect magnetic field lines. Expected particle motion is schematically presented on the figure (1) where electrons are confined by magnetic potential well while positive ions are thrown away from confinement area. However, it is sufficient to either switch direction of electric field or to change the curvature of magnetic field to confine ions and reject electrons. In the configuration of electric and magnetic field considered for purposes of this work, there is a confinement area for both species indicated by the arrows on the figure (26). In the case of

single particle, there is no self-consistent potential. The test particle moves in the external electric fields and external magnetic field. It means that charge assignement from equation (9) is zero and Poisson equation takes form of Laplace equation  $\vec{\nabla}^2\phi = 0$ .

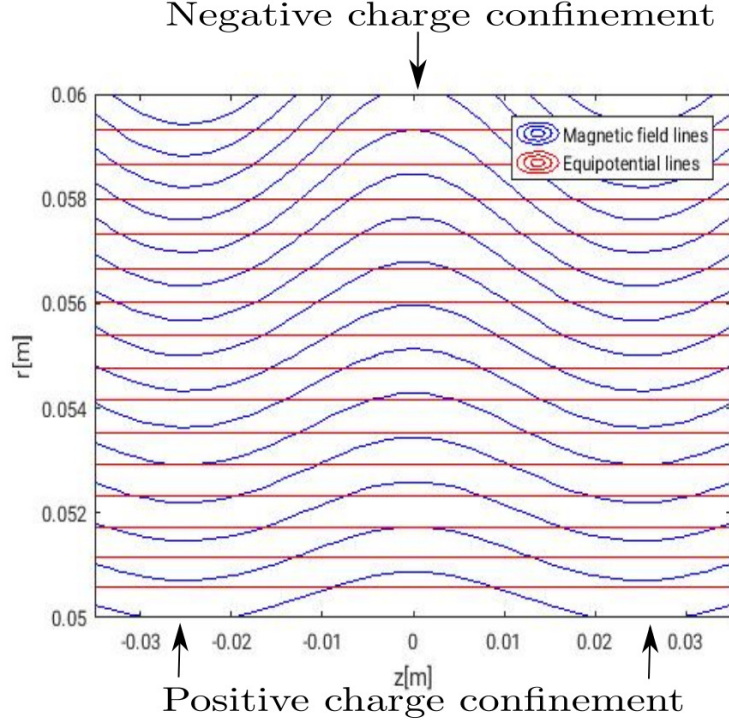


Figure 26: Equipotential and magnetic field lines

Trajectories of single particles positively and negatively charged were studied on figure (27). For both cases guiding center follow magnetic field lines and particles are confined at areas appropriate for the sign of the charge. However, in the following studies purely electron plasma will be studied. Moreover, Larmor radius is the same for both particles and particle rotate in opposite directions like expected. Both particles were initialised at the same position  $r_p = 0.055m$  and  $z_p = 0.016m$  and with zero velocity  $v_{\perp} = v_{\parallel} = 0$ . Numerical and physical parameters used in the calculation of particle trajectories are shown in the table (5). Dimensions of cylinder remains the same and are indicated in the table (2).

Table 5: Input parameters

$\Phi_1$	$\Phi_2$	$B_0$	$R$	$dt$	$n_{steps}$	$Q_{SIM}$
0V	30kV	0.2T	1.001	$10^{-12}s$	$10^4$	$\pm 1.55 \cdot 10^{-17}C$

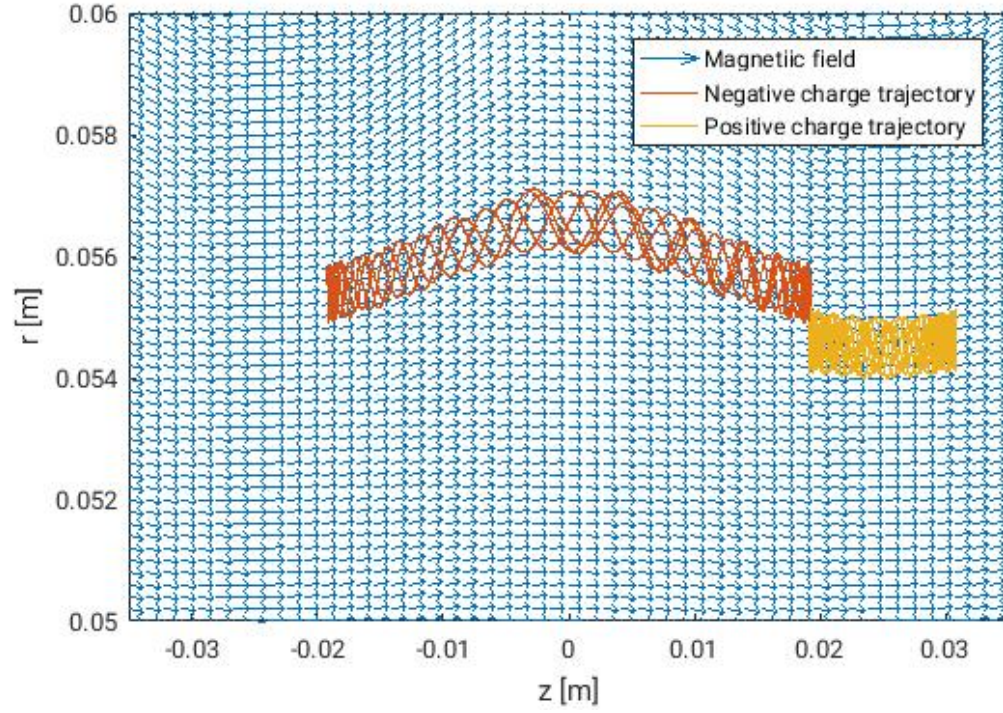


Figure 27: Positively and negatively charged particles trajectories

## 5 Electron plasma simulation

### 5.1 Electron plasma with $\frac{\omega_{ce}}{\omega_{pe}} = 8.81$

In the previous section it was found that single particle is trapped by the specific configuration of electric and magnetic field. The same effect is expected for simulation of more complex system with a large number of particles. Namely, one should notice that most of the particles are trapped at the confinement area while only a few of them can be found elsewhere. In this section initially cold electron plasma with zero velocity  $v_{\perp} = v_{\parallel} = 0$  is simulated. Initial positions of particles are specified by Hammerslay sequence (look at the figure (11)) between two radii  $R_{b1}$  and  $R_{b2}$  given in the table (6). Physical and numerical parameters used in the simulation are presented in the tables (6) and (7). Dimensions of cylinder remains the same and are indicated in the table (2).

Table 6: Physical parameters

$\Phi_1$	$\Phi_2$	$B_0$	$R$	$n_0$	$R_{b1}$	$R_{b2}$
0V	30kV	0.2T	1.001	$5 * 10^{15} m^{-3}$	0.051m	0.053m

Table 7: Numerical parameters

$dt$	$n_{steps}$	$N_{SIM}$	$n_z$	$n_r$
$10^{-11} s$	$10^4$	$10^4$	50	50

According to the normalised equations (4), (5) and (6), the nonneutral plasma frequency  $\omega_{pe} = \sqrt{\frac{n_0 e^2}{m_e \epsilon_0}}$  and the cyclotronic frequency  $\omega_{ce} = \frac{q_{SIM} B_0}{m_{SIM}}$  are physical quantities defined by input parameters from table (6). For considered magnetic field and density, the frequencies ratio is  $\frac{\omega_{ce}}{\omega_{pe}} = 8.81$ . It means that electron plasma is at the regime at which cyclotronic motion dominates over the collective effects and the nonneutral plasma evolution can be approximately considered as a collection of single particles. The second important parameter derived from the input parameters is the number of steps per one cycle of cyclotronic motion. For the considered case this parameter is  $N_{cyc} = \frac{T_c}{dt} = 18$ . The initial and final particles distribution is shown on the histograms on the figures (28) and (29). Initially, electrons

are distributed uniformly. According to the figure (28), particles are trapped in the middle of the domain but appropriate configuration of fields also occurs at the edges at  $z = \pm \frac{L}{2}$  where cyclic boundary conditions were applied. It means that every particle leaving the domain at one of the boundaries  $z = \pm \frac{L}{2}$  is put back on the opposite side with unchanged velocity. This constraint is not necessary in radial direction because particles are confined by the magnetic field configuration.

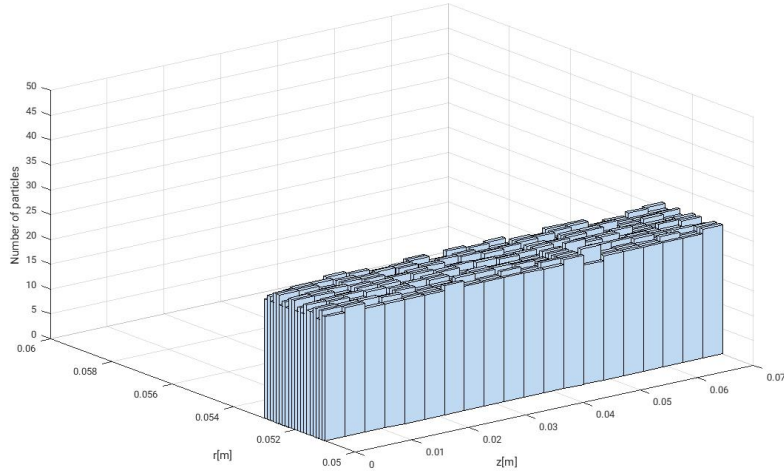


Figure 28: Initial particles positions

The density of charge in the confinement areas results in the small deformation of equipotential lines. The effect of charge displacement on the configuration of electromagnetic field is presented on the figure (30). The effect of charge density on equipotential lines is small because  $\frac{\omega_{ce}}{\omega_{pe}} = 8.81$ .

Potential, kinetic and total energy for electron plasma are described by the formulas from equations (43), (44) and (45). They are used as diagnostics to check if simulation is working correctly. Kinetic energy of nonneutral plasma is calculated as a sum of kinetic energies of single particles. However, potential energy can be simply calculated as a dot product of charge assignment and potential vector from equation (9).

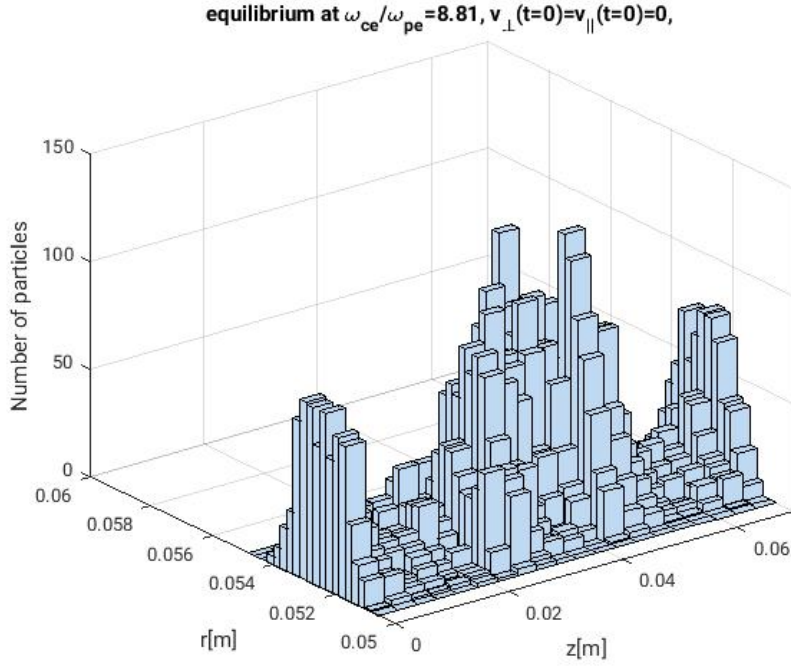


Figure 29: Final particles positions

$$\epsilon_p = \frac{1}{2} \int_V \rho \phi dV = \frac{1}{2} \sum_i Q_i \phi_i \quad (43)$$

$$\epsilon_k = \frac{1}{2} \sum_p m_p v_p^2 \quad (44)$$

$$\epsilon_t = \epsilon_p + \epsilon_k \quad (45)$$

Variation of potential, kinetic and total energy for  $\omega_{ce} dt = 0.35$  is presented on the figure (31).

According to the figure (31), the total energy converge to a certain value which is different compared to the initial total energy which is  $2.25 \cdot 10^4 J$ . However, by decreasing the timestep one can reduce the error between final and initial energy. The effect of timestep on this error is presented on the figure (32).

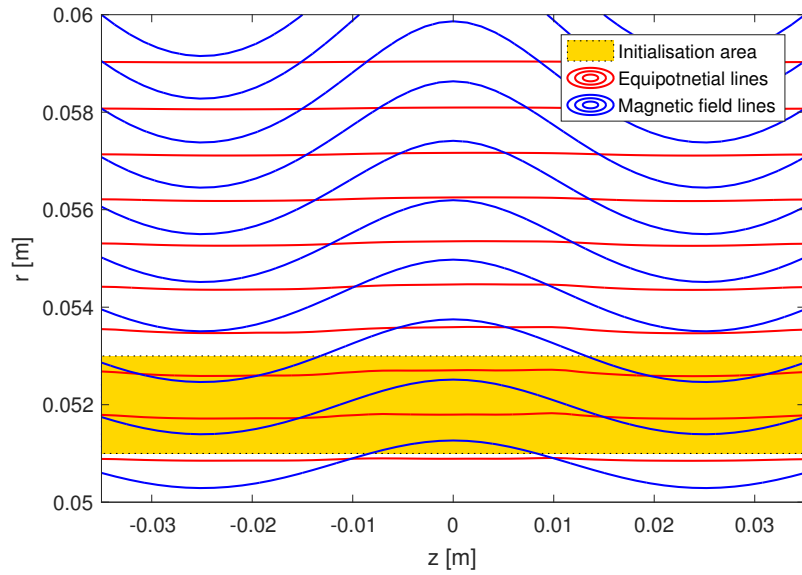


Figure 30: Equipotential and magnetic field lines

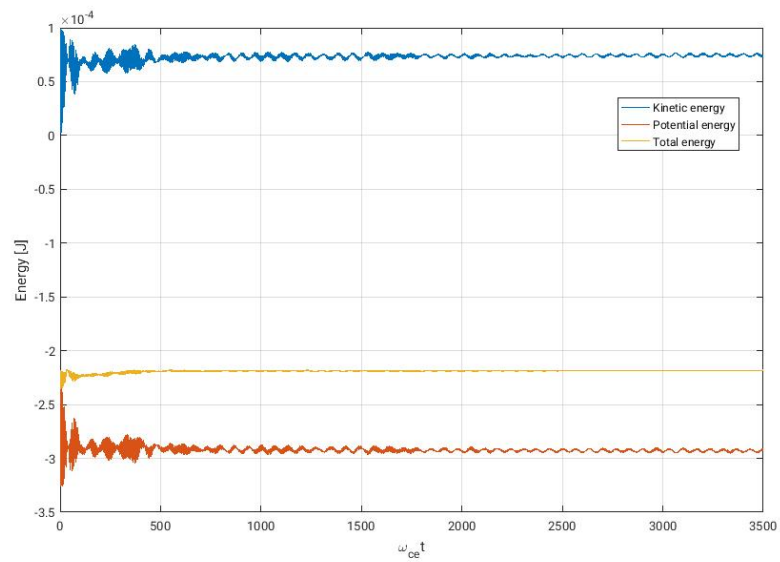


Figure 31: Potential, kinetic and total energy variation



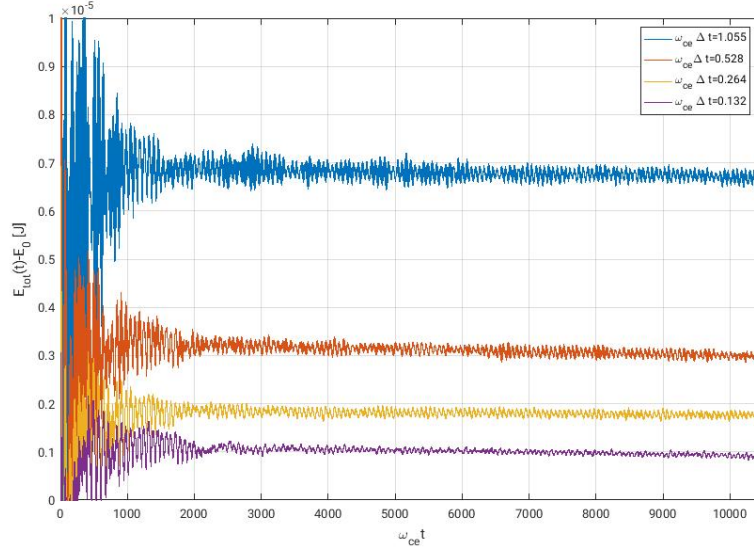


Figure 32: Error of energy conservation

## 5.2 Electron plasma with $\frac{\omega_{ce}}{\omega_{pe}} = 3.11$

Second example of electron plasma studied in this work is the one higher density with respect to the previous example, thus a lower ratio between the cyclotronic frequency and the electron plasma frequency  $\frac{\omega_{ce}}{\omega_{pe}} = 3.11$ . Physical and numerical parameters used in the simulation are presented in the tables (8) and (9). Initial and final distribution of particles are presented on the

Table 8: Physical parameters

$\Phi_1$	$\Phi_2$	$B_0$	$R$	$n_0$	$R_{b1}$	$R_{b2}$
0V	30kV	0.2T	1.001	$4 * 10^{16} m^{-3}$	0.054m	0.055m

Table 9: Numerical parameters

$dt$	$n_{steps}$	$N_{SIM}$	$n_z$	$n_r$
$8 * 10^{-12} s$	$10^4$	$10^4$	50	50

histograms (33) and (34). Particles are still confined in the expected regions.

Moreover, due to the higher density with respect to the previous example the deformation of equipotential lines become significant like indicated on the figure (35). The asymmetry in the equipotential lines come from a small asymmetry in final particles distribution. One can conclude that electron plasma is not in the equilibrium. The equilibrium is not reached even for longer simulation times.

The energy conservation was also studied for this case. The surprising result is that the total energy is not conserved due to a constant growth of kinetic energy. Kinetic, potential and total energies are presented on figure(36). The total energy growth is shown on figure (37). The system is isolated and changes in kinetic energy should be compensated by changes in potential energy. It is possible that this unexpected result come from bad choice of numerical parameters. The best way to solve this problem would be to make a step back and test the code (convergence tests) on simple examples with respect to each parameter separately. Especially, convergence of the particle mover using Boris method should be tested. The second possible reason is that the energy is measured in the wrong way. From figure (36), one can notice that while kinetic energy is growing the potential energy is slightly decreasing. There may be a normalisation issue which can not be solved due to the lack of time.

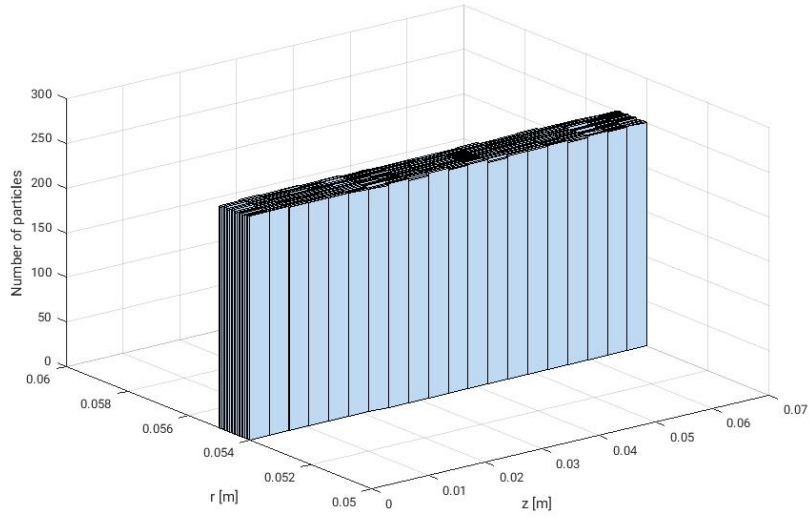


Figure 33: Initial particles positions

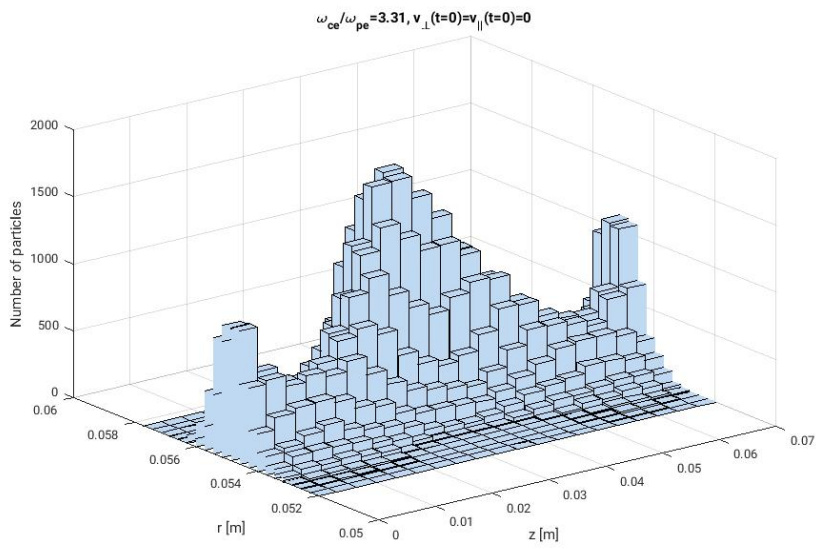


Figure 34: Final particles positions

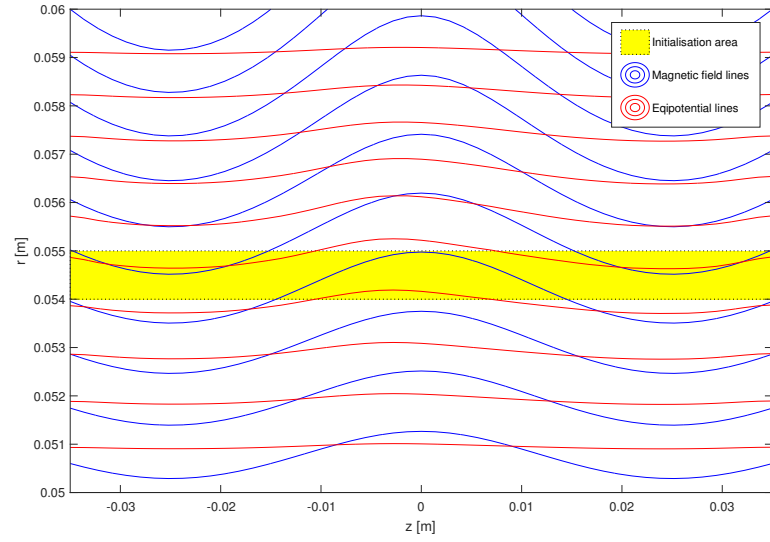


Figure 35: Equipotential and magnetic field lines

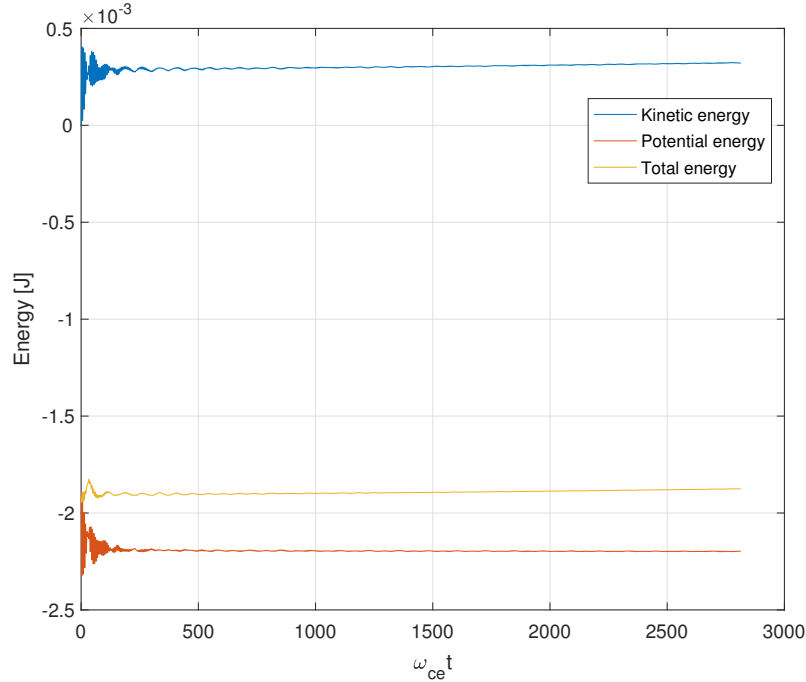


Figure 36: Potential, kinetic and total energy variation

## 6 Conclusions

In this work, the model for nonneutral plasma was built. The geometry of the magnetron electron gun (MIG) was approximated by cylinder. Electrostatic particle in cell (PIC) model was applied for electron motion simulation which consists of two equations of motion (1), (2) and poisson equation (3). Normalised form of those equations was derived and implemented. Poisson equation was solved with finite elements method (FEM) and tested on two examples with known analitical solutions. In particle pusher implementation Boris method was used what allow to split electron motion to acceleration due to electric field and rotation due to magnetic field. Single particle tests were done for the mirror magnetic field configuration and penning trapping. For both cases electrons were moving in expected way. Finally, the validity of the code was tested on the complex system of electron plasma with  $\frac{\omega_{ce}}{\omega_{pe}} = 8.81$ . Electrons were confined by Penning mechanism and reached equilibrium indicated by energy conservation. Moreover, it was found that the

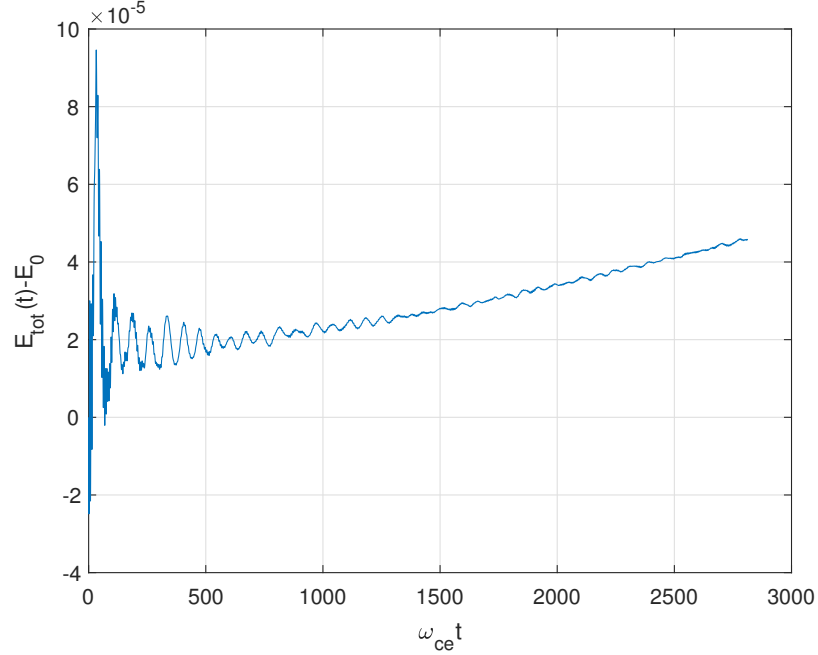


Figure 37: Error of energy conservation

difference between final and initial energy is decreasing when time increment is getting smaller. On the other hand, the electron plasma with  $\frac{\omega_{ce}}{\omega_{pe}} = 8.81$  did not conserve a total energy even though it was well confined by Penning mechanism. This surprising result needs to be studied in the future. First of all, one needs to find a reason why this growth occurs which can be a bad choice of numerical parameters or a wrong way of energy measurements. As soon as the code will be checked one can start to develop a code in terms of geometry of the system or more complex nonneutral plasma systems including electron beam and secondary electrons coming from ionization. A future goal would be to study in more details the mechanisms of electron trapping and possible instabilities that could lead to sudden loss of electron confinement.

## References

- [1] Charles K. Birdshall and A. Bruce Langdon. *Plasma physics via computer simulation*. McGraw-Hill, New York, 1985.
- [2] R. C. Davidson. *Physics of Nonneutral Plasmas*. Addison-Wesley, 1990.
- [3] Ioannis Gr. Pagonakis, Bernhard Piosczyk, Jianhua Zhang, Stefan Illy, Tomasz Rzesnicki, Jean-Philippe Hogge, Konstantinos Avramidis, Gerd Gantenbein, Manfred Thumm, and John Jelonnek. Electron trapping mechanisms in magnetron injection guns. *Phys. Plasmas*, 23(023105), 2016.